PAPER

Check for updates

An experimental investigation of vibrational, optical, and dielectric properties of Li–Mg ferrite for potential high-frequency and optoelectronic applications

Ibtihel Soudani, [a] Najoua Weslati, [b] Sami Znaidia, [c] Abderrazek Oueslati, [*b] Abdelhedi Aydi [a] and Kamel Khirouni[d]

Spinel lithium ferrites hold considerable significance in technological applications. Numerous investigations are conducted to explore the mechanisms underlying their properties. This work aims to detail the vibrational, optical, dielectric, thermodynamic, and magnetic properties of the $LiMg_{0.5}Fe_2O_4$ compound. Infrared and Raman spectroscopy further indicate the formation of the spinel phase in the samples. The optical study reveals a direct band gap with semiconducting characteristics, approximately 2.15 eV, with a low Urbach energy, indicating minimal disorder. Furthermore, precise calculations of thermodynamic parameters, including entropy change (ΔS), enthalpy change (ΔH), and free energy of activation (ΔF), provide additional insights into the properties of the compound. High dielectric permittivity values, reaching around 10^5, are observed and attributed to the Maxwell–Wagner interfacial polarization mechanism. The remanent magnetization ($M_r = 0.97$ emu g^{-1}) and coercive field ($H_C = 4.55$ Oe) extracted from the M–H loop are both notably low, clearly indicating the superparamagnetic nature of the sample. Our results show that $LiMg_{0.5}Fe_2O_4$ ferrite is a promising candidate for applications in multifunctional devices.

1 Introduction

Over the past few decades, nanotechnology has emerged as a powerful engine driving innovation across various scientific and industrial domains. In particular, nanomaterials have shown immense potential to revolutionize fields such as electronics, energy storage, environmental sensing, and biomedical engineering by providing enhanced physical, chemical, and functional properties compared to their bulk counterparts.[1–3] Among these, transition-metal-based spinel ferrites have garnered significant attention due to their unique blend of magnetic, electrical, dielectric, and catalytic properties, which can be precisely adjusted through chemical substitution, particle size control, and synthesis methods.[4–7]

Spinel ferrites have a general chemical formula of MFe_2O_4, where M represents a divalent metal ion (*e.g.*, Mg^{2+}, Zn^{2+}, Ni^{2+}, Co^{2+}, *etc.*). They crystallize in a cubic close-packed oxygen

lattice, with metal ions occupying tetrahedral (A) and octahedral (B) sites.[8] This type of spinel ferrite exhibits perfect stoichiometry that fulfills a cation-to-anion ratio of 3/4. However, the most well-known spinel ferrites, namely maghemite (α-Fe_2O_3), are the currently available spinel minerals and deviate from this stoichiometry.[9] This indicates the presence of nonstoichiometric spinel, depending on the overall cation-to-anion ratio. Hypostoichiometry is observed when the cation-to-anion ratio is less than 3/4, while spinels display hyperstoichiometry when the ratio exceeds 3/4.[9] These characteristics can be easily tuned for various applications by adjusting factors such as particle size, composition, and synthesis conditions.

These materials demonstrate high electrical resistivity, low eddy current losses, and moderate saturation magnetization, making them highly suitable for advanced electronics and energy storage systems.[10–12] Their properties enhance device efficiency and drive innovations in computing, clean energy, and electronic technologies.[13–15] Furthermore, their environmental friendliness, affordability, and chemical stability encourage their use in memory and catalysis.[13–16] Their small particle size and high surface-to-volume ratio further enhance their performance, making them ideal candidates for next-generation magnetoelectronic applications.[17]

Recently, lithium-based spinel ferrites have emerged as promising multifunctional materials due to their improved

[a]*Laboratory of Multifunctional Materials and Applications (LaMMA), LR16ES18, Faculty of Sciences of Sfax, University of Sfax, BP 1171, 3000 Sfax, Tunisia. E-mail: ebtihel.soudani@gamil.com*

[b]*Laboratory for Spectroscopic Characterization and Optics of Materials, Faculty of Sciences, University of Sfax, B. P. 1171, 3000 Sfax, Tunisia*

[c]*Department of Physics, Faculty of Science, King Khalid University, Abha, Saudi Arabia*

[d]*Laboratory of Physics of Materials and Nanomaterials Applied to the Environment, Faculty of Sciences of Gabès Cited Erriadh, 6079 Gabès, Tunisia*

electrical and magnetic properties. The incorporation of Li^+ into the spinel structure affects cation distribution, which can enhance charge carrier mobility and magnetic exchange interactions.[18,19] Lithium ferrites are studied for use in magnetic hyperthermia, energy storage devices, sensors, and high-density data storage technologies.[20–22] In particular, the substitution of lithium ferrites with divalent or trivalent cations can significantly modify their structural distortion, dielectric behavior, and magnetic performance.[23–25]

Despite extensive studies on lithium ferrites, the compound $LiMg_{0.5}Fe_2O_4$ remains relatively underexplored in terms of its complete physicochemical and functional characterization.[26] Previous studies have either focused on structural or electrical properties in isolation, without integrating insights from vibrational, optical, dielectric, and magnetic investigations.[26,27] Moreover, most reported synthesis methods rely on sol–gel or hydrothermal techniques, which, although effective, are often expensive and unsuitable for large-scale fabrication.

In this work, we focus on $LiMg_{0.5}Fe_2O_4$ synthesized *via* the solid-state reaction route, a cost-effective and scalable technique that allows the preparation of phase-pure materials with high crystallinity. The present study goes beyond simple parameter reporting by offering a comprehensive and correlated investigation of the structural, morphological, optical, dielectric, and magnetic characteristics of $LiMg_{0.5}Fe_2O_4$. To the best of our knowledge, such a multifaceted approach to this composition has not been reported in the literature. Additionally, the magnetic properties of $LiMg_{0.5}Fe_2O_4$ reveal a saturation magnetization value comparable to other ferrites, positioning the material as a strong candidate for microwave device applications.

The originality of this study lies not only in the integrated and comparative analysis of multiple physicochemical properties but also in its effort to correlate microstructural features with dielectric and magnetic performance. By revealing structure–property relationships, we aim to contribute new understanding of this under-investigated material and expand its potential for future use in electronics, sensors, and magneto-electric devices.

2   Experimental

The $LiMg_{0.5}Fe_2O_4$ compound is prepared using the solid-state process, employing high-purity precursors lithium carbonate (Li_2CO_3, 99.9% Sigma-Aldrich), magnesium oxide (MgO, 99.5% Sigma-Aldrich), and ferric oxide (Fe_2O_3, 99.5% Sigma-Aldrich). These are dehydrated in the oven at 150 °C to remove water bubbles and moisture. The stoichiometric amounts of precursors are weighed and mixed. Once the mixture is ready, it is ground in an agate mortar. The product is calcined at 850 °C for 7 hours at a rate of 5 °C min^{-1}, and then cooled at 3 °C min^{-1}. The resulting powder is ground and compressed into pellets to create a uniform, pure, compact crystalline sample. Following this, the pellets are sintered at 1100 °C with a heating rate of 5 °C min^{-1} for 2 hours.

X-ray diffraction (XRD) is conducted using Cu Kα radiation (λ = 1.5406 Å) with a scan range 2θ (10°–100°), step size (0.02°),

a dwell time per step (1 s), and generator settings of 40 kV, 30 mA to verify phase formation. The diffraction peaks are indexed according to the ICDD database, and structural refinement is performed using FullProf software. Surface morphology is analyzed through scanning electron microscopy (SEM) after gold coating. Transmission electron microscopy is carried out on an FEI Tecnai F20 to obtain images.

Raman scattering measurements are conducted at room temperature using a SENTERRA (Bruker) spectrometer, which is equipped with a 540 nm green laser for excitation. The system is calibrated with a silicon standard, yielding a spectral resolution of approximately 1 cm^{-1}. Spectra are collected over a range of 100–800 cm^{-1} to examine the vibrational characteristics of the sample. Fourier-transform infrared (FTIR) spectra are recorded using a Bruker Tensor 27 spectrophotometer across a range of 400–2400 cm^{-1}, achieving a spectral resolution of 4 cm^{-1} after accumulating 32 scans. Calibration is performed utilizing a standard polystyrene film. UV-vis-NIR spectroscopy is also employed to evaluate the optical characteristics of the produced compounds. Dielectric measurements are conducted over a wide frequency range (100 Hz to 7 MHz) using an Agilent 4294A impedance analyzer, with an applied alternating electric signal of 50 mV and silver paste electrodes on both sides of the pellet. Magnetic hysteresis measurements are executed using a SQUID magnetometer at ambient temperature (300 K), with magnetic fields reaching up to 10 T.

3   Results and discussion

3.1   X-ray diffraction, morphological, vibrational, and optical study

The $LiMg_{0.5}Fe_2O_4$ X-ray diffraction pattern carried out at ambient temperature and presented in Fig. 1a, exhibits sharp and well-defined reflection peaks indexed to the cubic spinel-phase lattice structure with a space group $Fd\bar{3}m$. The absence of extraneous peaks depicts the high phase purity and crystalline quality of the synthesized material. The detailed structural parameters obtained from the Rietveld refinement are already presented in this study.[27]

The SEM micrograph of $LiMg_{0.5}Fe_2O_4$ is shown in Fig. 1b, highlighting a surface with well-defined polygonal and polyhedral grains. The average grain size is about 2.27 μm.[27]

The TEM image in Fig. 1c shows that the particles have a non-uniform shape and tend to clump together. This clumping is mainly due to magnetic interactions between nanoparticles, which have high surface energy and large surface-to-volume ratios.[28] The average particle size is about 30–32 nm, which aligns well with the size determined by previous XRD analysis.[27]

A vibrational analysis is conducted using infrared and Raman spectroscopies to obtain deeper insights into the crystal structure. The observed bands are identified by comparison with previously reported experimental and theoretical vibrational studies of similar compounds.[29]

Experimental IR and Raman spectra of ferrite spinel material $LiMg_{0.5}Fe_2O_4$ are reported in Fig. 2 and 3.

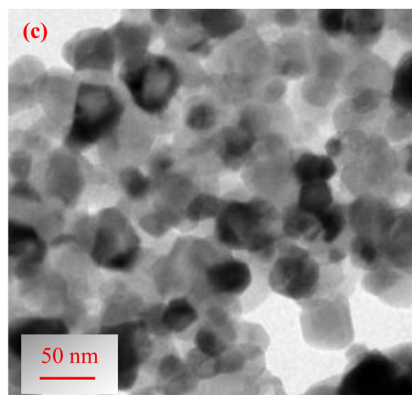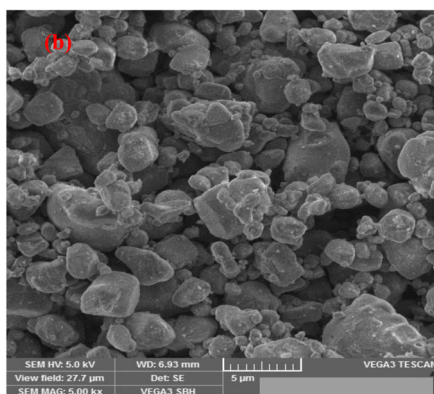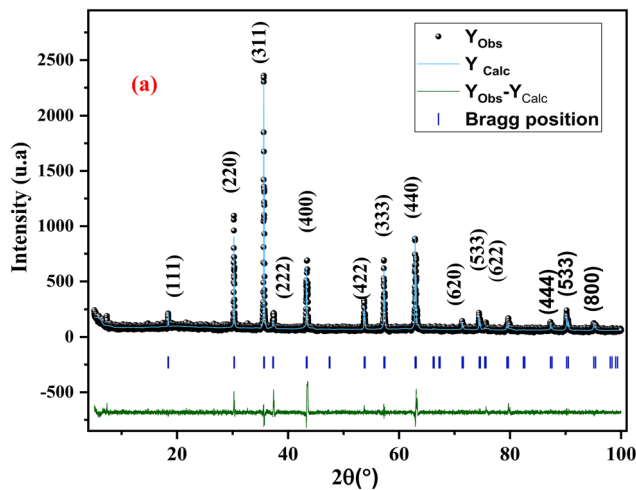**Fig. 1** The XRD pattern with Rietveld analysis (a), SEM micrograph (b), and TEM figure (c) of $LiMg_{0.5}Fe_2O_4$.

Fig. 2 Raman of $LiMg_{0.5}Fe_2O_4$.
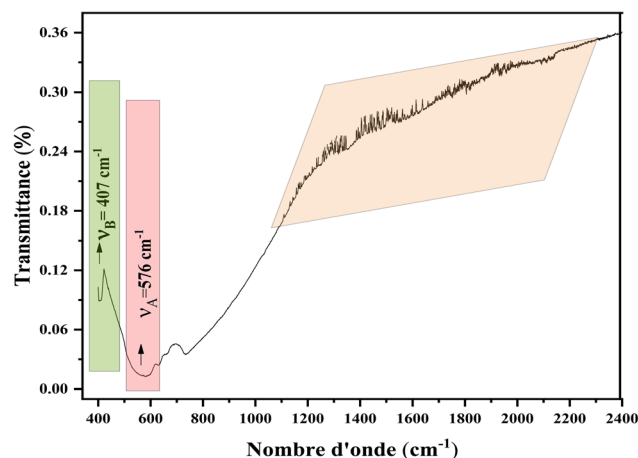
Fig. 3 FTIR of $LiMg_{0.5}Fe_2O_4$.

The Raman spectrum at room temperature, recorded in the range of 53 cm^{-1} to 898 cm^{-1} and shown in Fig. 2, displays a broad band with two distinct peaks at 500 cm^{-1} and 696 cm^{-1}. These peaks correspond to the symmetrical stretching vibrations of oxygen atoms relative to the metal ions in octahedral sites.[30] They are associated with the A_{1g} (1) and A_{1g} (2) vibrational modes in the $Fd\bar{3}m$ spectroscopic symmetry. Two other peaks of moderate intensity appear at 347 cm^{-1} and 263 cm^{-1}. These are attributed to the external translation modes T_{2g} (3) and T_{2g} (2), respectively. These peaks result from the symmetrical and asymmetrical bending of oxygen atoms in the
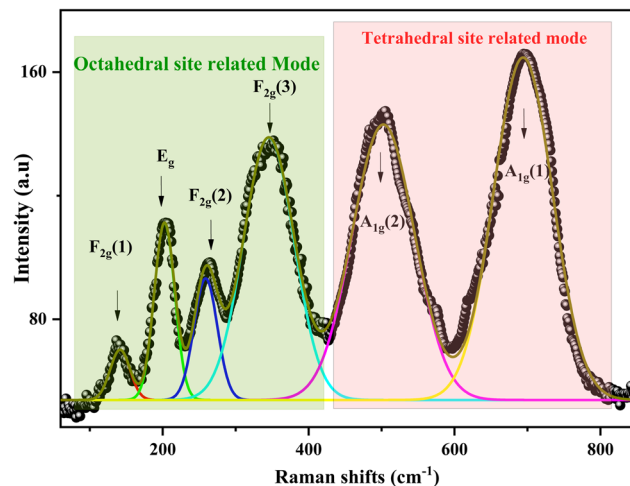
tetrahedral site binding.[30] A Raman peak observed at 204 cm^{-1} is associated with the E_g mode, corresponding to the symmetrical bending of oxygen atoms at the tetrahedral site.[30] Finally, a band at 131 cm^{-1} is attributed to the T_{2g} (1) mode, linked to ions in the tetrahedral site.[30] Compared to related compositions, the slight shifts in peak positions reflect the specific Mg content in our material.[31–34]

In summary, all active Raman bands of $LiMg_{0.5}Fe_2O_4$ correspond to the theoretical vibrational modes of the $Fd\bar{3}m$ space group, validating the formation of $LiMg_{0.5}Fe_2O_4$ ferrite spinel nanoparticles.[30]

The Fourier-transform infrared (FTIR) spectrum, recorded in the wavenumber range of 400–2400 cm^{-1} at room temperature, provides complementary vibrational information about the $LiMg_{0.5}Fe_2O_4$ material. As shown in Fig. 3, two absorption bands are observed. The first appears at 407 cm^{-1}, and the second at 576 cm^{-1}, indicating the presence of metal oxides. These metal–oxygen bonding peaks are attributed to the stretching vibrations of the cation–anion bonds in octahedral

sites (μ_B) and tetrahedral sites (μ_A), respectively.[35] This confirms the formation of the $LiMg_{0.5}Fe_2O_4$ spinel compound.

According to information obtained by some researchers for other spinel nanoparticles, the small bands in the range of 1150 to 2200 cm^{-1} may be related to the symmetric and asymmetric stretching vibrations of water (O–H). It is caused by the physical adsorption of water on nanoparticles present on the surface of solids.[36]

FTIR spectra are used to calculate the threshold energy (E_{th}). This energy is derived from the electronic transition and threshold wavenumber (v_{th}), where the absorption spectra reach a maximum (limiting) value.

The threshold energy can be calculated using the following equation:[37]

$$E_{th} = hcv_{th} \tag{1}$$

where h means the Planck constant (6.626×10^{34} J) and the velocity of light is in the order of 3×10^8 m s^{-1}. The E_{th} value is tabulated in Table 1.

It is well established that the wavenumbers ($v_{1,2}$) of the infrared-active phonon modes are intrinsically linked to the force constant (F) and the reduced mass (m) of the metal–oxygen bond. The force constants for the tetrahedral A-site (K_t) and octahedral B-site (K_o) are computed utilizing the following formula:[38]

$$K_{t,o} = 4\pi^2 C^2 v_{1,2}{}^2 \mu \tag{2}$$

Elastic constants measure how well a crystal resists external stresses. This is important for ferrites in industry because their elastic properties determine the strength of the material under different stress conditions. In research, studying these properties allows us to understand inter-atomic and inter-ionic forces

and their thermal behavior. Modi *et al.* developed a method using infrared spectroscopy and structural data to calculate elastic parameters for spinel ferrite and garnet systems.[39] Waldron's rule states that C_{11} equals C_{12} for materials with cubic symmetry. The volume modulus (B), Young's modulus (E), stiffness modulus (G), Poisson's ratio (σ), and the velocities of longitudinal (V_1), transverse (V_t), and average waves (V_m) are calculated using specific formulas[39] are calculated and tabulated in Table 1.

The Pugh criterion allows us to distinguish the brittle or ductile behavior of the studied material.[40] The ratio of bulk modulus (B) to rigidity modulus (G) is an indicator according to this criterion. If the ratio is less than 1.75, the material is considered brittle and ductile if it is greater. Using the Ledbetter and Datta models, we calculated that the B/G ratio for $LiMg_{0.5}Fe_2O_4$ is 1.98. This value clearly shows that the sample is ductile.

Lastly, the Debye temperature simplifies thermal capacity integration by indicating the temperature at which the maximum lattice vibrations occur. The formula that Waldron supplied is used to determine it:[40]

$$\Theta = \frac{\hbar C}{k} v_a = 1.438 v_a, \quad v_a = \frac{v_1 + v_2}{2} \tag{3}$$

Here, v_a represents the mean wavenumber of the bands, h is Planck's constant, k is Boltzmann's constant, and C means the speed of light. For ferrite materials, the constant $\hbar C/k$ is taken as 1.438.

The Debye temperature can also be determined in another way, from the average velocity V_m, using Anderson's formula:[40]

$$\theta_D = \frac{h}{k} \left(\frac{3q\rho_0 N_A}{4\pi M} \right)^{1/3} V_m \tag{4}$$

Table 1 The elastic parameters for the $LiMg_{0.5}Fe_2O_4$ sample

	$LiFe_2O_4$ (ref. 41)	$LiMg_{0.5}Fe_2O_4$
The threshold energy E^{th} (eV)	—	0.162
The force constants for the A-site K_t (Nm^{-1})	273	243
The force constants for the A-site K_o (Nm^{-1})	177	121
Stiffness constant C_{11} (GPa) $C_{11} = \dfrac{K_a}{a}$	270	218
The average constant K_a (Nm^{-1}) $K_a = \dfrac{K_T + K_O}{2}$	225	182
Bulk modulus B (GPa) $B = \dfrac{1}{3}(C_{11} + 2C_{11}) = C_{11}$	270	218
Transverse wave velocity V_1 (ms^{-1}) $V_1 = \sqrt{\dfrac{C_{11}}{\rho_{X\text{-ray}}}}$	8017	9150
Longitudinal wave velocity V_t (ms^{-1}) $V_t = \dfrac{V_1}{\sqrt{3}}$	4628	5282
Rigidity modulus G (GPa) $G = \rho_{X\text{-ray}} \times Vt^2$	139	110
Poisson's ratio σ $\sigma = \dfrac{3B - 2G}{6B + 2G}$	0.262	0.2
Young's modulus E (GPa) $E = (1 + \sigma)^2 \times G$	350.8	398.4
Mean wave velocity V_m (ms^{-1})	5138	5864.090
$V_m = \left(\dfrac{1}{3} \left(\dfrac{2}{V_t^3} + \dfrac{1}{V_1^3} \right) \right)^{-\frac{1}{3}}$		
Debye temperature θ (K)	706	707
Debye temperature θ_D (K)	775	790

In this context, N_A, ρ_0, M, and q are Avogadro's number, density, and molecular mass number of atoms per unit formula, respectively. Table 1 lists all the parameter values.

Recent data on the elastic properties of stoichiometric $LiFe_2O_4$ allow a direct comparison with $LiMg_{0.5}Fe_2O_4$, as summarized in Table 1. While $LiMg_{0.5}Fe_2O_4$ shows a slightly lower C_{11}, suggesting reduced stiffness, its bulk modulus and Poisson's ratio remain comparable, indicating similar compressibility and bonding character to $LiFe_2O_4$.[41] These results demonstrate that the hyperstoichiometric structure does not significantly affect mechanical performance and may even improve the material's dielectric behavior. Thus, $LiMg_{0.5}Fe_2O_4$ appears as a promising alternative for multifunctional applications.

During the high-temperature solid-state synthesis of $LiMg_{0.5}Fe_2O_4$, Mg vacancies are likely formed within the crystal lattice. To compensate for the loss of Mg ions, some Fe^{3+} ions located at the B-sites are reduced to Fe^{2+} and migrate (hop) toward the Mg (A) sites. This hopping disturbs the local equilibrium, prompting neighboring ions to rearrange and stabilize the lattice. As a result, the vibrational frequencies associated with the BO_6 octahedral sites are significantly affected, as evidenced by Raman and FTIR analyses.

Furthermore, this ion hopping process leads to the coexistence of Fe^{2+} and Fe^{3+} ions, which enhances the electronic conduction by facilitating electron hopping between these mixed valence states. This mechanism is further supported by the observed decrease in relaxation time and the temperature-dependent increase in electrical conductivity in our measurements.[40]

The absorbance measurements of our sample, which encompasses wavelengths from 200 nm to 1500 nm within the UV-visible-NIR range are illustrated in Fig. 4a. This spectrum shows an absorption band that peaks at wavelengths shorter than 500 nm: (i) The photo-excitation of electrons from the valence band (VB) to the conduction band (CB) and (ii) the electronic transitions of the iron (Fe^{3+}) transitions (from $3d^5$ to $3d^4\ 4s^1$) are the two main mechanisms responsible for this absorption, according to the earlier reports on spinel ferrite materials.[27,28] The primary property of materials regarded as a potential promoter for optoelectronic applications is their optical band gap (E_g). It can be efficiently calculated using the reflectance data and its derivative, based on the strongest diffraction peak, as shown in the inset Fig. 4b; the (E_g) value is 2.05 eV. Also, the Kubelka–Munk function approach is then used to estimate the (E_g) for the sample more accurately:[42]

$$F(R) = \frac{(1-R)^2}{2R} = \frac{\alpha}{S} \qquad (5)$$

where α is the absorption coefficient, S is the scattering factor, and R is the reflection factor. Since $LiCd_{0.5}Fe_2O_4$,[43] $LiNi_{0.5}Fe_2O_4$,[44] and $LiMg_{0.5}Fe_2O_4$ (ref. 27) exhibit a direct band, the synthesized compound also shows a similar band nature. Thus, by plotting the square of the absorption coefficient $(\alpha h\nu)^2$ as a function of the photon energy ($h\nu$), the optical band gap (E_g) is determined from the energy axis intersection point of the
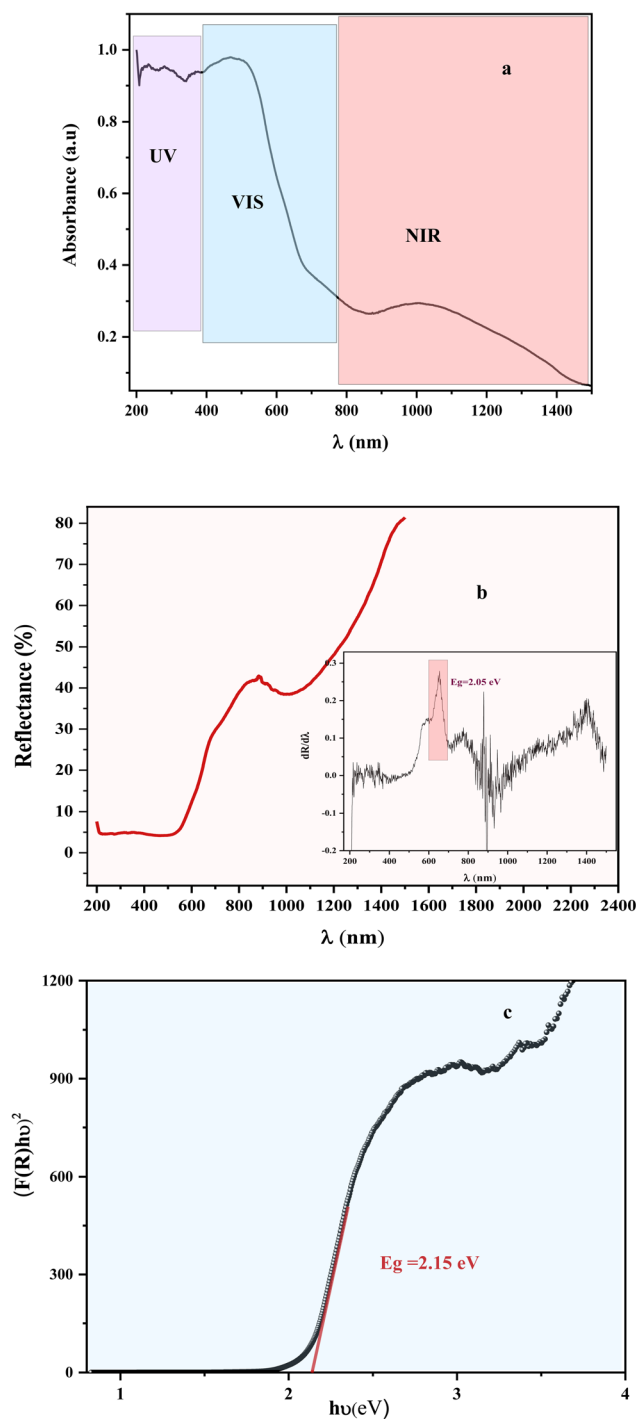

Fig. 4 Absorbance spectra (UV-VIS-NIR) *versus* λ (a), reflectance spectra *versus* λ (b). The inset shows the $dR/d\lambda$ *versus* λ curve and $(F(R)h\nu)^2$ *versus* $h\nu$ (c) for the $LiMg_{0.5}Fe_2O_4$ sample.

tangent on the linear part, as illustrated in Fig. 4c. The value strongly agrees with the value taken from the $dR/d\lambda$ spectra.

A direct and narrower optical band gap of 2.15 eV is also observed for $LiMg_{0.5}Fe_2O_4$, compared to 2.8 eV for $LiFe_2O_4$.[41] This value lies within the typical semiconductor range and exceeds the 1.6–1.9 eV reported for other spinels such as $CoFe_2O_4$ or $MnFe_2O_4$,[45] indicating a more favorable response to

visible-light absorption. As a result, $LiMg_{0.5}Fe_2O_4$ appears highly suitable for optoelectronic and photocatalytic applications, including photovoltaics and photodetectors.

The band gap value is 2.15 eV, which is higher than the energy required for water separation ($E > 1.23$ eV). This can be responsible for better charge separation and increased photocatalytic activity under visible light (absorption capacity in the visible spectrum).[29]

The Urbach energy (E_U) is a key optical parameter that indicates the presence of impurities, structural disorders, and defects in the material.[30] It can be calculated using the photon energy ($h\nu$) with the following equation:[46]

$$\alpha = A \exp(h\nu/E_U) \tag{6}$$

where A represents a constant. Taking the natural logarithm of the above equation, the relationship can be linearized as follows:[46]

$$\ln \alpha = \ln A + \frac{h\nu}{E_U} \tag{7}$$

As represented in Fig. 5, by the slope of the linear region in the ($\ln(\alpha)$ versus $h\nu$) plot, the E_U value is obtained from the inclined portion of this plot and is equal to 0.270 eV which is markedly lower than values reported for $Mg_{0.6}Ni_{0.4}Cr_2O_4$ (2.14 eV), $Mg_{0.6}Cu_{0.4}Cr_2O_4$ (1.86 eV),[47] or $CoFe_2O_4$ and $MnFe_2O_4$ (0.94 and 1.20 eV, respectively).[48]

Such a small value of E_U indicates that the material is structurally ordered with a low density of defect states in the electronic structure.

The penetration depth (δ) shall define how deeply the incident light or radiation penetrates the material. It gives insight into the interaction between the material and electromagnetic (EM) waves. The penetration depth could be estimated based on the expression using the absorption coefficient $\alpha(\lambda)$:[49]

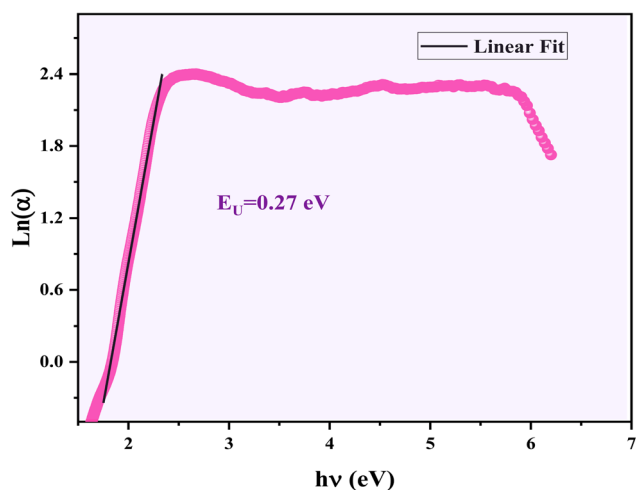$$\delta = \frac{1}{\alpha(\lambda)} \tag{8}$$

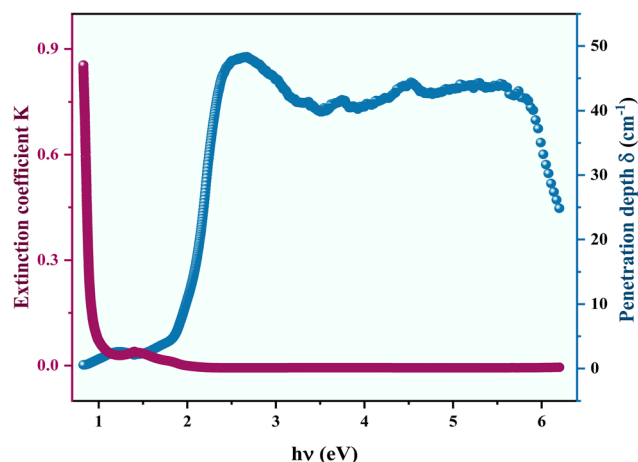**Fig. 5** Variation of $\ln(\alpha)$ versus $h\nu$.

Fig. 6 Evolution of the penetration depth δ and the optical extinction K versus $h\nu$.

We have shown the variation of δ in Fig. 6. It is evident that the penetration depth significantly decreases in the location of the strong absorption as the photon energy increases, indicating that the input light might be mightily absorbed. Furthermore, the latter outcome can be explained by the decrease in incident photon energy close to the surface, which could impact the quantity of nearby Fe^{3+} ions.[50] The extinction coefficient k conveys the drop in EM wave intensity once the wave is allowed to enter the material. It can be determined by applying the following equation:[49]

$$k = \frac{\alpha\lambda}{4\pi} \tag{9}$$

The extinction coefficient k's variation with photon energy $h\nu$ is depicted in the same Fig. 6. It is evident that when ($h\nu$) increases, our ceramic's extinction coefficient k diminishes. These results suggest that the $LiMg_{0.5}Fe_2O_4$ sample can be an optoelectronic sensor due to its strong UV absorption.[50]

The refractive index (n) is determined by a complex interaction between the incident light and the atomic structure of the $LiMg_{0.5}Fe_2O_4$ sample, which is determined according to the ensuing equation, with k is the extinction coefficient:[51]

$$n(\lambda) = \frac{(1+R)}{(1-R)} + \sqrt{\frac{4R}{(1-R)^2} + (k(\lambda))^2} \tag{10}$$

Fig. 7 represents the experimentally measured refractive index in the spectral region of small absorption that approximates the application of Cauchy's equation:[51]

$$n(\lambda) = n_0 + \frac{n_1}{\lambda^2} + \frac{n_2}{\lambda^4} \tag{11}$$

The Cauchy model fits the experimental data rather well. Table 2 regroups the fitted values of the Cauchy parameters n_0, n_1, and n_2. Also, the optical constants are studied using the Wemple–DiDomenico (WDD) with the single-oscillator model, applying eqn (17):[51]
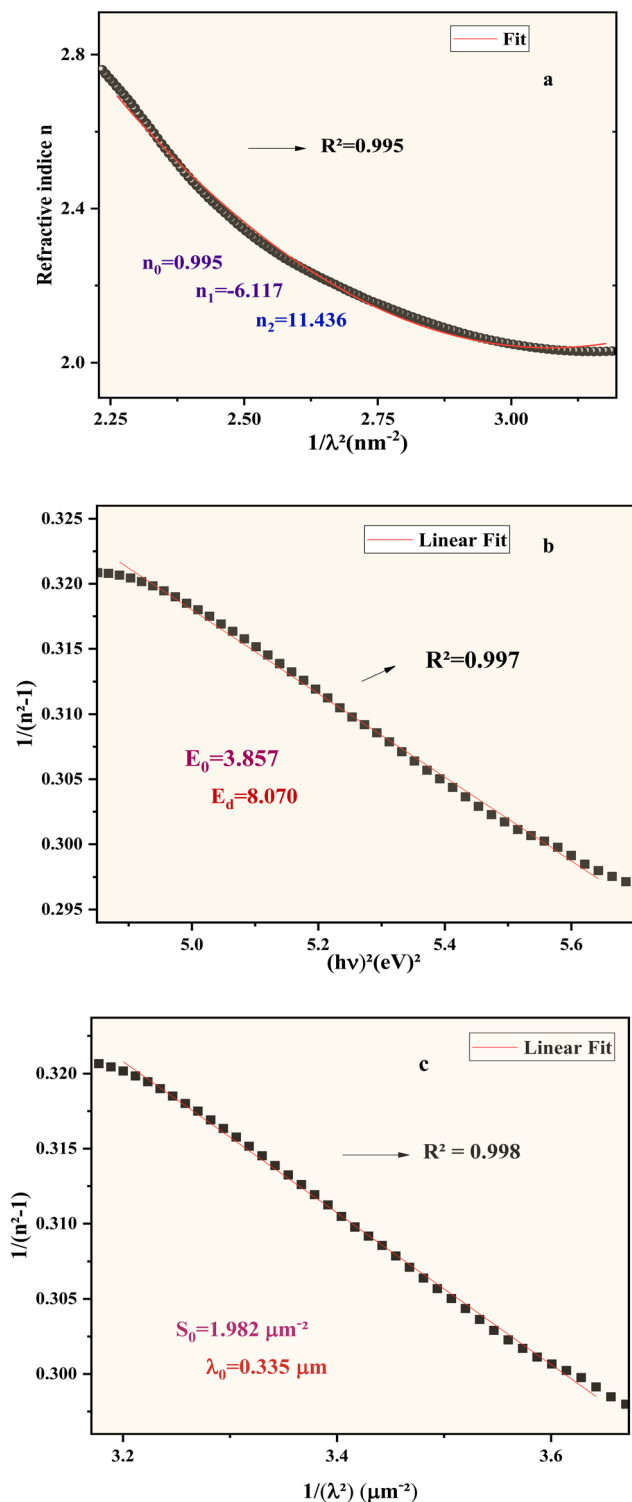
Fig. 7 The plot of $(n^2 - 1)^{-1}$ versus (λ^{-2}) (a) evolution of $(n^2 - 1)^{-1}$ versus $(h\nu)^2$ (b) and n versus (λ^{-2}) (c).

$$n^2 - 1 = \frac{E_0 E_d}{E_0^2 - (h\nu)^2} \tag{12}$$

Fig. 7 shows the linear fitting of the data, and parameters such as the effective single oscillator energy (E_0) and dispersion

Table 2 The optical parameters for the LiMg$_{0.5}$Fe$_2$O$_4$ sample

	$n_0 = 0.995$
	$n_1 = -6.117$
The Cauchy model fit	$n_2 = 11.436$
The effective single oscillator energy E_0	3.857
The dispersion energy E_d	8.070
The mean oscillator wavelength λ_0 (μm)	0.335
The oscillator intensity S_0 (μm^{-2})	1.982
The moment M_{-1}	2.097
The moment M_{-3}	0.141

energy (E_d), which reflect the strength of interbond optical transitions, have been determined. These parameters have been obtained from the fit's intercept (E_0/E_d) and slope ($-1/E_0 E_d$) and are summarized in Table 2. Furthermore, this model also allows us to study the refractive index to gauge the mean oscillator wavelength (λ_0) and oscillator intensity (S_0) of the non-Born-Oppenheimer Fluctuating Oscillations sample. The parameters are resolved *via* the succeeding equation:[51]

$$n^2 - 1 = \frac{S_0 \lambda_0^2}{1 - \left(\frac{\lambda_0}{\lambda}\right)^2} \tag{13}$$

As depicted in Fig. 7c, S_0 and λ_0 are obtained from the straight-line fit of $[(n(\lambda)^2 - 1)]^{-1}$ *vs.* λ^{-2}. The findings are listed in Table 2.

The WDD model establishes relations between the oscillator energy (E_0), dispersion energy (E_d), and moments M_{-1} and M_{-3} of the optical spectrum by the following equation $E_d^2 = (M_{(-1)})^3/M_{(-3)}$, respectively.[52,53] The latter values are gathered in Table 2.

Similar values have been reported for other stoichiometric spinel ferrites. The close correspondence of these parameters supports the optical reliability and relevance of LiMg$_{0.5}$Fe$_2$O$_4$ within the ferrite family for optoelectronic applications.[51] This comparison suggests that hyperstoichiometric substitution, as in LiMg$_{0.5}$Fe$_2$O$_4$, preserves the general optical behavior observed in stoichiometric spinel ferrites, while potentially enhancing tunability for targeted optoelectronic applications.

Fig. 8a shows the trend of the optical conductivity (σ_{opt}) *versus* wavelength (λ) for LiMg$_{0.5}$Fe$_2$O$_4$. The optical conductivity is computed from eqn (20),[49] which relates to the material's optical properties:[50]

$$\sigma_{opt} = \frac{\alpha(\lambda) n(\lambda) C}{4\pi k(\lambda)} \tag{14}$$

The optical conductivity shows three peaks at $\lambda_1 = 681$ nm, $\lambda_2 = 815$ nm, and $\lambda_3 = 883$ nm. This demonstrates that more excited electrons are generated by photon energy at specific wavelengths. Devices using optoelectronics may take advantage of this outcome. Our material can be utilized to choose particular frequencies in the visible spectrum by acting as an optical filter. The complex dielectric constant is expressed as:[49]
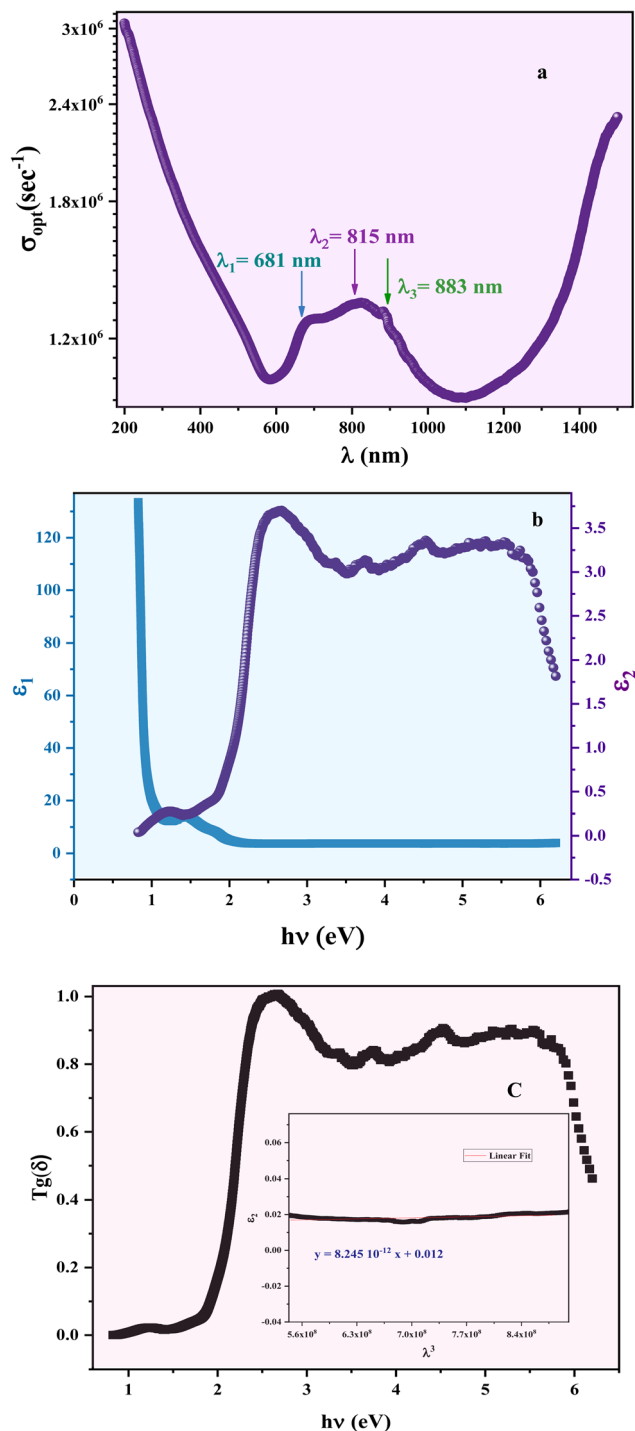
Fig. 8 Optical conductivity σ_{opt} as a function of λ (a), real and imaginary parts of the dielectric constant of versus $h\nu$. Represents the energy loss of the light (c). The inset imaginary part of the dielectric constant as a function of λ^3 (c).

$$\varepsilon(\omega) = \varepsilon_1(\omega) - i\varepsilon_2(\omega) \quad (15)$$

It is an important parameter to outline the optical properties of the studied sample. The real part (ε_1) and the imaginary part (ε_2) of the dielectric constant are numerically computed with the aid of an equation, as follows:[49]

$$\varepsilon_1 = (n(\lambda))^2 - (k(\lambda))^2 \quad (16)$$

$$\varepsilon_2 = 2n(\lambda)K(\lambda) \quad (17)$$

Fig. 8b shows ε_1 and ε_2 vary with photon energy ($h\nu$). The real part ε_1 spectrum copes very well with the refractive index, chiefly because of the small values of the extinction coefficient ($k(\lambda)$). The imaginary part, on the contrary, ε_2, is strongly influenced by $k(\lambda)$. In the near-infrared region, its imaginary part is described by the classical relation:[52]

$$\varepsilon_2 = C_1\lambda^3 \quad (18)$$

The inset of Fig. 8c displays the variation of ε_2 versus λ^3, where the obtained constant value of C_1 equals 3.611×10^{-14} nm^{-3}.

The loss factor ($t_g\delta$) is defined by the most common relation, which is the ratio between the imaginary part and the real part of the permittivity ($\varepsilon_2/\varepsilon_1$).[49] Fig. 8c depicts its variation concerning photon energy ($h\nu$). This thorough examination of the dielectric properties offers valuable insights into the materials' low energy loss and optical performance.

3.2 Dielectric, thermodynamic, and magnetic results

The study of complex Modulus is adopted to gain a deeper understanding of the dielectric relaxation process at different temperatures and frequencies and to eliminate any phenomena related to various interfaces and electrode levels.

The evolution of the imaginary part of the Modulus (M'') as a function of frequency at different temperatures is depicted in Fig. 9a. As shown, each spectrum is distinguished by a peak that appears at a specific frequency, referred to as the relaxation frequency (f_r). In the low-frequency part ($f < f_r$), charge carriers undergo hopping between sites to cover long distances, while at higher frequencies ($f > f_r$), charge carriers are more confined within their potential, thus hindering localized movement. At the relaxation frequency ($f \approx f_r$), a smooth transition between long-distance and short-distance movement is commonly observed.[54,55] The peaks shift towards higher frequency regions with increasing temperatures, indicating the activation of the relaxation process. As the temperature rises, charge carriers move at an increased speed.[56] This can be explained by the impact of grains on the activation of the hopping phenomena, consistent with the work of Abdallah et al.[56] From the relaxation peak, we extracted the relaxation frequency (f_r) and presented its variation versus temperature in Fig. 9b. We inferred an Arrhenius variation of $\log(f_r)$ versus $1000/T$ according to the following equation:[57]

$$f_r = f_0 \exp(-E_a/k_B T) \quad (19)$$

where T, k_B, E_a, and f_0 are the temperature, Boltzmann's constant, activation energy, and constant, respectively. The activated energy is in the order of 160 meV. The obtained value is in agreement with that derived from impedance analysis, with minor discrepancies likely arising from the frequency ranges used in the respective spectra.[27] This suggests that
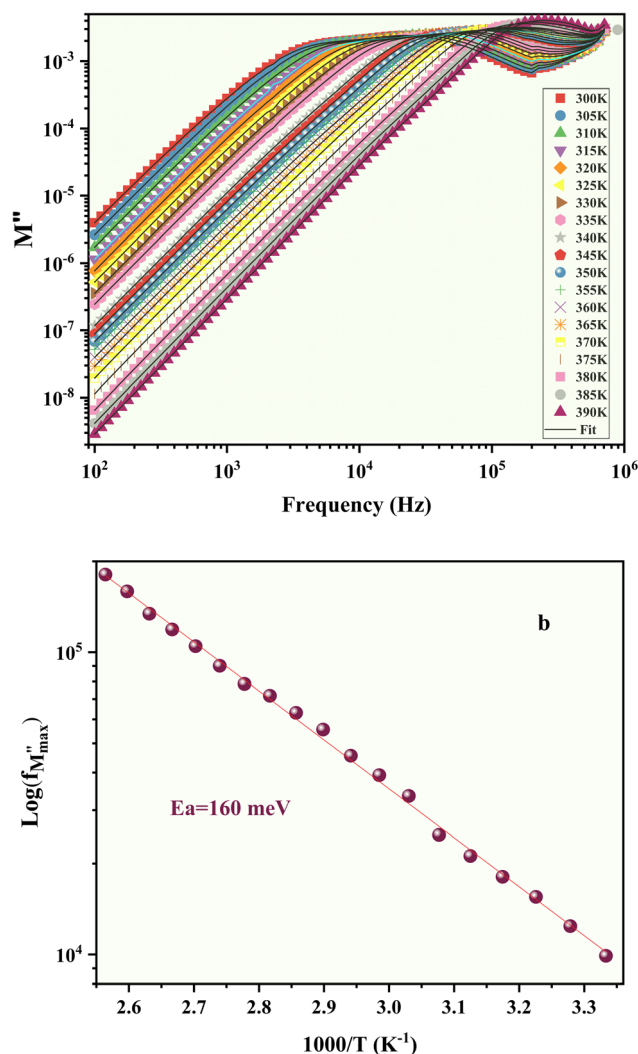
Fig. 9 The imaginary part of the modulus plot as a function of frequency at different temperatures (a), with black solid lines showing the fit of the recording data using relation (22). The Arrhenius curve log($f_{M''_{max}}$) *versus* the inverse of temperature for LiMg$_{0.5}$Fe$_2$O$_4$ sample (b).

similar energy barriers are involved in both the relaxation and conduction processes, indicating that the mobile charge carriers experience comparable activation energies.[9]

The relaxation time (τ) is consistent with the Gibbs free energy (ΔG) using the Eyring hypothesis. It can be expressed by the subsequent expression:[58]

$$\tau = \left(\frac{h}{k_B T}\right)\exp\left(\frac{\Delta G}{RT}\right) \tag{20}$$

where h, R, and ΔG are the Planck constant, the universal gas constant, and the Gibbs free energy, respectively. Besides, ΔG is correctly related to the enthalpy ΔH and entropy ΔS by the following relation:[58]

$$\Delta G = \Delta H - T\Delta S \tag{21}$$

Substituting this expression into the relaxation time equation, τ can be expanded as follows:[58]

$$\tau = \left(\frac{h}{k_B T}\right)\exp\left(\frac{\Delta H}{RT}\right)\exp\left(\frac{-\Delta S}{R}\right) \tag{22}$$

Fig. 10 presents a plot of log($\tau \times T$) against $1000/T$, which displays a linear trend. The entropy change (ΔS) is determined from the intercept, while the enthalpy change (ΔH) correlates with the slope of the fitted line. Their values are $\Delta H = 1.470$ cal mol^{-1} and $\Delta S = -6.737$ cal mol^{-1} K^{-1}. The negative entropy value (ΔS) indicates dipole–dipole interactions.[58] This suggests that in the active state, the molecules are closely packed. This method provides insights into the molecular movements and interactions in the studied substance.[58]

The variation of the real (ε') and imaginary (ε'') parts of the dielectric permittivity as a function of frequency and temperature is presented in Fig. 11. It is evident that both dielectric components exhibit high values in the low-frequency range. This behavior is primarily due to localized charge dynamics, specifically the electron exchange between Fe^{2+} and Fe^{3+} ions, combined with polarization effects resulting from ion displacement. As the frequency increases beyond 10^4 Hz, these slower mechanisms can no longer keep pace with the oscillating electric field. This suggests that our material, LiMg$_{0.5}$Fe$_2$O$_4$, is a promising candidate for energy storage at low frequencies under applied alternating electric fields, offering increased capacity.[59] Conversely, at higher frequencies, ε' and ε'' decrease, enhancing the energy storage capability.[60,61] This behavior is controlled by the Maxwell–Wagner theory intended for interfacial polarization.[62] Also, it is well-aligned with Koop's phenomenological theory of dielectric materials.[63] Based on these models, the LiMg$_{0.5}$Fe$_2$O$_4$ structure consists of grains with high conductivity surrounded by poor conductor bulk boundaries where the electrons navigate amongst them for the exchange mechanism. These grain boundaries act as obstacles that restrict the mobility of electrons, leading to a reduction in inter-grain conductivity.
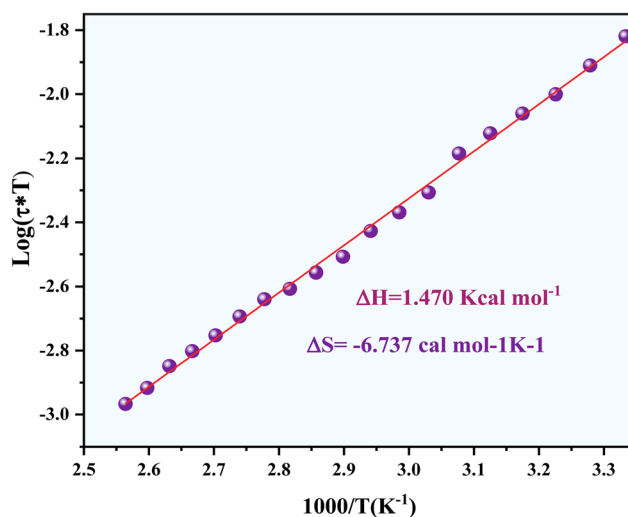

Fig. 10 The Arrhenius curve log($\tau \times T$) *versus* the inverse of temperature for LiMg$_{0.5}$Fe$_2$O$_4$ sample.
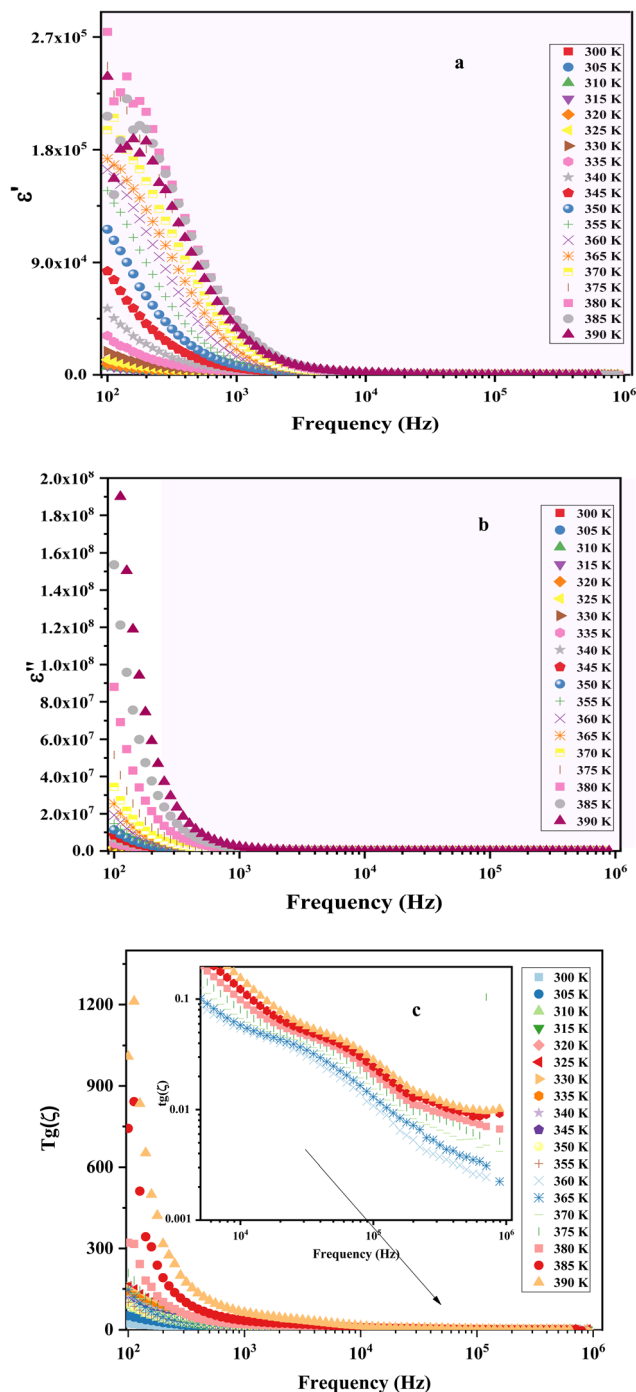
Fig. 11 (a) The dielectric data of the real permittivity (ε'), (b) the recorded dielectric data of the imaginary permittivity (ε''), (c) loss tangent *versus* frequencies at several temperatures [300–390 K] for the synthesized ferrite.

From our complex permittivity data, we calculate the loss tangent as:[64]

$$t_g(\xi) = \frac{\varepsilon''}{\varepsilon'} \tag{23}$$

Consistent with general ferrite behavior (as represented in Fig. 11c), we observe that $t_g(\xi)$ decreases with increasing

frequency, as polarization mechanisms (*e.g.*, electrode/interface polarization and ionic hopping) cannot follow the rapidly oscillating field at higher frequencies.[64] For instance, at room temperature in our LiMg$_{0.5}$Fe$_2$O$_4$ sample, $t_g(\xi)$ decreases from relatively high values at low frequencies (100 Hz) to much lower values by the upper end of our measurement range.

Our measured $t_g(\xi)$ at MHz frequencies (≈ 0.05 or lower between 1–7 MHz) suggests that LiMg$_{0.5}$Fe$_2$O$_4$ is a promising candidate for specific capacitor-like applications involving ferrite-based dielectrics.[65] For comparison, LiFe$_2$O$_4$ has been reported to exhibit a prominent peak in $\tan \delta$ due to domain wall resonance, associated with the hopping frequency between Fe^{3+} and Fe^{2+} ions.[41] Compared to this behavior, the flatter and lower $t_g(\xi)$ values of LiMg$_{0.5}$Fe$_2$O$_4$ in the MHz range indicate a reduced dielectric loss profile. As reported in the literature, achieving low $t_g(\xi)$ in the microwave range depends on optimized microstructure and composition.[66] With appropriate densification and defect management, LiMg$_{0.5}$Fe$_2$O$_4$ has the potential to meet the requirements for microwave applications, as supported by the results of the magnetic study.[67]

Fig. 12 illustrates the variation in the capacity to store electric charge with frequency at different temperatures. A high capacitance value is observed in the lower frequency range, which may be attributed to interface states that follow an AC signal.[57] Conversely, as the frequency increases, the capacity decreases, typically due to the presence of material traps.

These results suggest that the examined sample has numerous potential applications in various technological fields, including high-frequency applications, such as lithium-ion batteries, electronic devices, fuel cells, and low-temperature ceramics suitable for co-firing.[29–40]

Fig. 13 presents the magnetic hysteresis (M–H) curve of the LiMg$_{0.5}$Fe$_2$O$_4$ sample, measured at room temperature under a magnetic field up to 10 T. At ambient temperature, the hysteresis curve exhibits a narrow loop, indicating minimal energy dissipation during the magnetization and demagnetization cycles. This low magnetic loss behavior suggests that
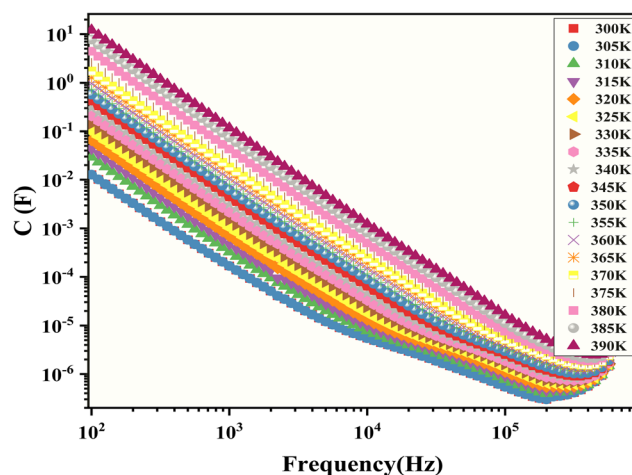

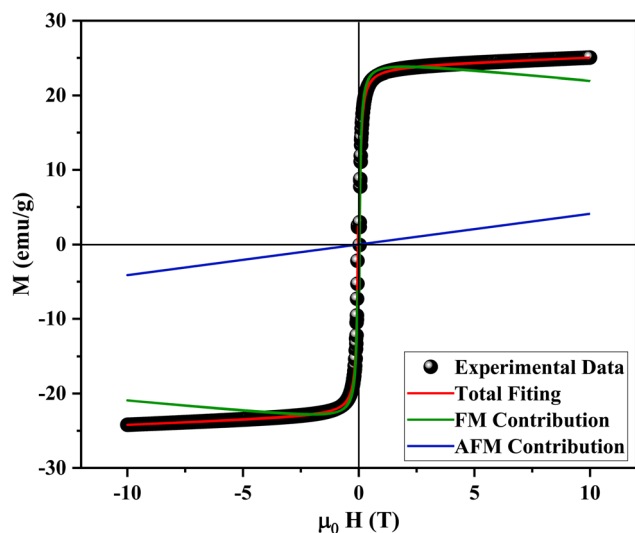Fig. 12 The variation of capacity (C) as a function of frequency at different temperatures.

Fig. 13 The hysteresis loops of LiMg$_{0.5}$Fe$_2$O$_4$ measured at 300 K.

LiMg$_{0.5}$Fe$_2$O$_4$ is a promising candidate for use in magnetic refrigeration technologies.[68]

To extract the main magnetic parameters such as saturation magnetization (M_s), remanent magnetization (M_r), and coercive field (H_C). The M–H curve is fitted using the following model:[28]

$$M(H) = 2 \frac{M_s^{FM}}{\pi} \times \arctan\left[\left(\frac{H \pm H_C}{H_C}\right) \times \tan\left(\frac{\pi}{2} \times \frac{M_r}{M_s^{FM}}\right)\right] + \chi H$$

(24)

In this equation, the first term corresponds to the ferromagnetic contribution, while the second term (linear) accounts for the antiferromagnetic and paramagnetic components.

The revealed magnetic measurements that LiMg$_{0.5}$Fe$_2$O$_4$ exhibits soft magnetic behavior, with a saturation magnetization M_s = 22.39 emu g^{-1}, remanent magnetization M_r = 0.97 emu g^{-1}, and coercivity H_C = 4.55 Oe. These low values of M_r and H_C are characteristic of superparamagnetic materials, indicating low energy loss and excellent response to weak external fields. In contrast, LiFe$_2$O$_4$ shows M_s = 51 emu g^{-1}, M_r = 23 emu g^{-1}, and a higher coercivity of H_C = 119 Oe, confirming a more magnetically rigid nature. The observed superparamagnetic behavior of LiMg$_{0.5}$Fe$_2$O$_4$, combined with its relatively large particle size (~2.27 μm) observed via SEM,[27] suggests strong potential for technological and biomedical applications. These include recording heads, transformers, induction cores, spintronic devices, microwave components,[28] as well as magnetic resonance imaging (MRI) contrast enhancement, hyperthermia treatment, and multifunctional magnetic tools for low-field environments.[29]

Furthermore, the effective magnetic moment n_B (μ_B) is estimated using the following relationship:[28]

$$n_B(\mu_B) = \frac{M_s M_W}{5585}$$

(25)

where M_W is the molar mass of the compound (g mol^{-1}). The result obtained is 0.78 μ_B.

To evaluate the material's potential for high-frequency microwave applications, the microwave resonance frequency (ω_m) is calculated using the following equation:[28]

$$\omega_m = \gamma 8\pi^2 M_s$$

(26)

where γ = 2.8 MHz Oe^{-1} is the gyromagnetic factor. The LiMg$_{0.5}$Fe$_2$O$_4$ compound has a frequency of 24.25 GHz, making it compatible with the S and C bands of microwaves. This value, comparable to those reported for other ferrites, demonstrates that this material is a strong candidate for radiofrequency and microwave devices.[29,30]

4 Conclusion

This study presents a detailed and systematic investigation of LiMg$_{0.5}$Fe$_2$O$_4$ ferrite synthesized via the solid-state reaction method, addressing the limited understanding of how Mg substitution affects its multifunctional properties. By combining advanced structural, vibrational, optical, magnetic, and dielectric characterizations, we reveal clear correlations between the material's microstructure and its electrical and magnetic behavior.

Notably, the observation of superparamagnetic behavior, along with a direct wide optical band gap (~2.15 eV) and colossal dielectric permittivity, highlights the potential of LiMg$_{0.5}$Fe$_2$O$_4$ for applications in microwave frequency devices, optoelectronics, and biomedical technologies such as hyperthermia treatment. The application of modulus formalism to analyze dielectric relaxation provides new insight into charge transport mechanisms that have been rarely explored in lithium ferrites.

Altogether, the results demonstrate that the hyperstoichiometric LiMg$_{0.5}$Fe$_2$O$_4$ does not compromise elastic performance, while simultaneously improving optical and magnetic performance. This multifunctional enhancement underscores its promise for advanced applications across optoelectronic and magnetic domains.

These findings not only enhance the fundamental understanding of non-stoichiometric spinel ferrites but also highlight LiMg$_{0.5}$Fe$_2$O$_4$ as a promising candidate material for next-generation multifunctional devices. Future research will concentrate on optimizing synthesis parameters and doping strategies to customize these properties for specific technological applications.

Data availability

The authors confirm that the data used to support the findings of this study are included within the article and are available from the corresponding author upon reasonable request.

Author contributions

Ibtihel Soudani: Writing – original draft, visualization, methodology, investigation, formal analysis. Najoua Weslati: Writing – review & editing, software, methodology, investigation. Sami

Znaidia: Validation, supervision, resources, project administration, methodology. Abderrazek Oueslati: Writing – original draft, supervision, validation, project administration. Abdelhedi Aydi: Writing – original draft, supervision, methodology, Kamel Khirouni: Writing – original draft, supervision, methodology.

Conflicts of interest

The authors declare that they have no known competing financial interests or personal relationships that could have appeared to influence the work reported in this paper.

Acknowledgements

References

1 S. Wang, X. Chen, K. Luo, H. Zhou, R. Li, P. He and S. Zhang, *J. Mater. Res. Technol.*, 2023, **27**, 5332–5339.

2 D. Zhang, D. Shi, F. Wang, D. Qian, Y. Zhou, J. Fu and S. Jiang, *J. Alloys Compd.*, 2023, **966**, 171536.

3 H. Yu, J. Huang, M. Zhao, J. Xu, M. Li and L. Kong, *J. Mol. Struct.*, 2024, **1316**, 139015.

4 N. Akhlaghi and G. Najafpour-Darzi, *J. Ind. Eng. Chem.*, 2021, **103**, 292–304.

5 D. Chen, Y. Li, X. Li, X. Hong, X. Fan and T. Savidge, *Chem. Sci.*, 2022, **13**, 8193–8202.

6 K. K. Kefeni, T. A. M. Msagati and B. B. Mamba, *Mater. Sci. Eng., B*, 2017, **215**, 37–55.

7 S. Soltani-Nezhad, A. Mashreghi, S. Hasani, Z. Daneshfar, M. T. Rezvan and A. Emami, *Mater. Chem. Phys.*, 2024, **323**, 129625.

8 A. E. Elkholy, F. E. T. Heakal and N. K. Allam, *RSC Adv.*, 2017, **7**, 51888–51895.

9 I. Soudani, K. B. Brahim, A. Oueslati, H. Slimi, A. Aydi and K. Khirouni, *RSC Adv.*, 2022, **12**, 18697–18708.

10 D. S. Mathew and R.-S. Juang, *Chem. Eng. J.*, 2007, **129**, 51–65.

11 S. B. Somvanshi, P. B. Kharat, M. V. Khedkar and K. M. Jadhav, *Ceram. Int.*, 2020, **46**, 7642–7653.

12 S. B. Somvanshi, S. A. Jadhav, S. S. Gawali, K. Zakde and K. M. Jadhav, *J. Alloys Compd.*, 2023, **947**, 169574.

13 K. K. Kefeni, B. B. Mamba and T. A. M. Msagati, *Sep. Purif. Technol.*, 2017, **188**, 399–422.

14 S. Moslemi, E. Mohebbi and S. Hasani, *Mater. Chem. Phys.*, 2024, **315**, 129015.

15 Z. Yin, X. Yin, Y. Feng, S. Huang, R. Zhang, X. Zhang and Y. Wu, *J. Alloys Compd.*, 2025, **1029**, 180776.

16 V. A. Bharati, S. B. Somvanshi, A. V. Humbe, V. D. Murumkar, V. V. Sondur and K. M. Jadhav, *J. Alloys Compd.*, 2020, **821**, 153501.

17 Q. Du and Z. Wang, *J. Alloys Compd.*, 2025, **020**, 179557.

18 S. B. Somvanshi, S. A. Jadhav, M. V. Khedkar, P. B. Kharat, S. D. More and K. M. Jadhav, *Ceram. Int.*, 2020, **46**, 13170–13179.

19 S. B. Somvanshi, S. R. Patade, D. D. Andhare, S. A. Jadhav, M. V. Khedkar, P. B. Kharat and K. M. Jadhav, *J. Alloys Compd.*, 2020, **835**, 155422.

20 S. Singhal, S. K. Barthwal and K. Chandra, *J. Magn. Magn. Mater.*, 2006, **306**, 233–240.

21 M. Ounacer, B. Rabi, A. Essoumhi, M. Sajieddine, B. F. O. Costa, M. Emo and M. Sahlaoui, *J. Alloys Compd.*, 2021, **854**, 156968.

22 M. Darvishi, S. Hasani, A. Mashreghi, M. Taghi Rezvan and A. Ziarati, *Mater. Sci. Eng., B*, 2023, **297**, 116754.

23 I. H. Gul and A. Maqsood, *J. Alloys Compd.*, 2008, **465**, 227–231.

24 S. P. Waghmare, D. M. Borikar and K. G. Rewatkar, *Mater. Today Proc.*, 2017, **4**, 11866–11872.

25 Y. Chen, Y. Guo, B. Xie, F. Jin, L. Ma, H. Zhang and N. Zhao, *Nat. Commun.*, 2024, **15**(1), 4334.

26 F. Gandomi, S. M. Peymani-Motlagh, M. Rostami, A. Sobhani-Nasab, M. Fasihi-Ramandi, M. Eghbali-Arani and M. R. Ganjali, *J. Mater. Sci. Mater. Electron.*, 2019, **30**, 19691–19702.

27 I. Soudani, F. N. Almutairi, I. Chaabane, A. Oueslati, A. Aydi and K. Khirouni, *J. Phys. Chem. Solids*, 2025, **201**, 112631.

28 A. Jeidd, M. Amghar, A. Mabrouki, A. Benali, A. Trabelsi, E. Dhahri and B. F. O. Costa, *RSC Adv.*, 2023, **13**, 12906–12916.

29 I. Soudani, K. B. Brahim, A. Oueslati, A. Aydi, K. Khirouni, A. Benali and M. A. Valente, *RSC Adv.*, 2023, **13**, 9260–9272.

30 J. Massoudi, M. Smari, K. Nouri, E. Dhahri, K. Khirouni, S. Bertaina and E. K. Hlil, *RSC Adv.*, 2020, **10**, 34556–34580.

31 M. D. Hossain, A. T. M. K. Jamil, M. S. Hossain, S. J. Ahmed, H. N. Das, R. Rashid and M. N. I. Khan, *RSC adv.*, 2022, **12**, 4656–4671.

32 A. M. Padhan, P. M. Rajaitha, S. Nayak, S. Hajra, M. Sahu, Z. Jagličić and H. J. Kim, *Mater. Chem. Front.*, 2023, **7**, 72–84.

33 M. P. Ghosh, R. Sonkar, G. Phukan, J. P. Borah and D. Chowdhury, *RSC adv.*, 2025, **15**, 12964–12981.

34 A. S. Alsubaie, R. Ali, M. M. Soliman, S. M. El-Bahy, M. H. Helal and A. U. Rahman, *Ind. J. Phys.*, 2025, 1–15.

35 R. D. Waldron, *Phys. Rev.*, 1955, **99**, 1727–1735.

36 G. Xian, S. Kong, Q. Li, G. Zhang, N. Zhou, H. Du and L. Niu, *Front. Chem.*, 2020, **8**, 177.

37 K. B. Modi, S. J. Shah, N. B. Pujara, T. K. Pathak, N. H. Vasoya and I. G. Jhala, *J. Mol. Struct.*, 2013, **1049**, 250–262.

38 R. S. Yadav, J. Havlica, J. Masilko, L. Kalina, J. Wasserbauer, M. Hajdúchová and Z. Kožáková, *J. Magn. Magn. Mater.*, 2015, **394**, 439–447.

39 K. B. Modi, P. Y. Raval, S. J. Shah, C. R. Kathad, S. V. Dulera, M. V. Popat and P. K. Jha, *Inorg. Chem.*, 2015, **54**(4), 1543–1555.

40 D. Bouokkeze, J. Massoudi, W. Hzez, M. Smari, A. Bougoffa, K. Khirouni and L. Bessais, *RSC Adv.*, 2019, **9**, 40940–40955.

41 M. Hashim, M. Tariq, M. M. Ismail, S. J. Salih, K. M. Batoo, M. Hadi and A. Nhlapo, *Ceram. Int.*, 2025, **51**, 874–884.

42 P. Kubelka, F. Munk and Z. Tech, *Phys*, 1931, **12**, 259–274.

43 O. Amorri, H. Slimi, A. Oueslati, A. Aydi and K. Khirouni, *Phys. B*, 2022, **639**, 414005.

44 J. Massoudi, D. Bouekkeze, A. Bougoffa, K. Khirouni, E. Dhahri and L. Bessais, *Adv. Powder Technol.*, 2020, **31**, 4714–4730.

45 A. Hadded, J. Massoudi, E. Dhahri, K. Khirouni and B. F. O. Costa, *RSC adv.*, 2020, **10**, 42542–42556.

46 J. Melsheimer and D. Ziegler, *Thin Solid Films*, 1985, **129**, 35–47.

47 T. S. Soliman, S. A. Vshivkov, M. M. Hessien and S. I. Elkalashy, *Soft Matter*, 2023, **19**(40), 7753–7763.

48 T. D. Thanh, T. T. N. Nha, T. T. H. Giang, P. H. Nam, D. N. Toan, D. T. Khan and P. T. Phong, *RSC adv.*, 2024, **14**(33), 23645–23660.

49 R. Mguedla, A. B. J. Kharrat, O. Taktak, H. Souissi, S. Kammoun, K. Khirouni and W. Boujelben, *Opt. Mater.*, 2020, **101**, 109742.

50 K. Souifi, O. Rejaiba, O. Amorri, M. Nasri, B. Alzahrani, M. L. Bouazizi and j. Khelifi, *J. Inorg. Organomet. Polym. Mater.*, 2022, **32**, 4515–4531.

51 S. Heni, S. Hcini, M. L. Bouazizi, L. HajTaieb, A. Dhahri and H. ben Bacha, *RSC adv.*, 2024, **14**(36), 26340–26353.

52 N. Tounsi, A. Barhoumi, F. Chaffar Akkari, M. Kanzari, H. Guermazi and S. Guermazi, *Vacuum*, 2015, **121**, 9–17.

53 Y. Janbutrach, S. Hunpratub and E. Swatsitang, *Nanoscale Res. Lett.*, 2014, **9**, 498.

54 T. Jadli, Y. Moualhi, A. Mleiki, H. Rahmouni, K. Khirouni and A. Cheikhrouhou, *J. Solid State Chem.*, 2021, **302**, 122378.

55 F. B. Abdallah, A. Benali, S. Azizi, M. Triki, E. Dhahri, M. P. F. Graça and M. A. Valente, *J. Mater. Sci. Mater. Electron.*, 2019, **30**, 8457–8470.

56 F. Hcini, S. Hcini, B. Alzahrani, S. Zemni and M. L. Bouazizi, *J. Mater. Sci. Mater. Electron.*, 2020, **31**, 14986–14997.

57 M. Mounir Bouzayani, M. B. Abdessalem, I. Soudani, A. Oueslati and A. Aydi, *RSC Adv.*, 2024, **14**, 12464–12474.

58 I. Soudani, M. Tliha, S. Znaidia, A. Oueslati, A. Aydi and K. Khirouni, *J. Solid State Chem.*, 2025, **341**, 125087.

59 M. M. Bouzayani, I. Soudani, M. B. Abdessalem, S. Znaidia, A. Oueslati and A. Aydi, *J. Mater. Sci. Mater. Electron.*, 2024, **35**, 1256.

60 M. F. Kotkata, F. A. Abdel-Wahab and H. M. Maksoud, *J. Phys. Appl. Phys.*, 2006, **39**, 2059.

61 S. B. Yahya and B. Louati, *J. Alloys Compd.*, 2021, **876**, 159972.

62 K. S. Chikara, A. K. Bera, A. Kumar and S. M. Yusuf, *ACS Appl. Electron. Mater.*, 2023, **5**, 2704–2717.

63 Y. Moualhi, H. Rahmouni and K. Khirouni, *Phys. B*, 2021, **616**, 413129.

64 N. Singh, A. Agarwal, S. Sanghi and S. Khasa, *J. Magn. Magn. Mater.*, 2012, **324**, 2506–2511.

65 J. Boonlakhorn, J. Manyam, S. Krongsuk, P. Thongbai and P. Srepusharawoot, *RSC adv.*, 2021, **11**, 25038–25046.

66 R. R. Mishra and A. K. Sharma, *Crit. Rev., Solid State Mater. Sci.*, 2016, **41**, 217–255.

67 V. P. Krylov, R. A. Chirkov, M. O. Zabezhailov and A. M. Khramov, *Meas. Tech.*, 2024, **67**, 143–150.

68 N. Amri, J. Massoudi, K. Nouri, M. Triki, E. Dhahri and L. Bessais, *RSC Adv.*, 2021, **11**, 13256.